BIOMIMETICS

A biologically inspired, flapping-wing, hybrid aerial-aquatic microrobot

Yufeng Chen,[1,2]* Hongqiang Wang,[1,2] E. Farrell Helbling,[1,2] Noah T. Jafferis,[1,2] Raphael Zufferey,[3] Aaron Ong,[1,2,4] Kevin Ma,[1,2] Nicholas Gravish,[4] Pakpong Chirarattananon,[5] Mirko Kovac,[3] Robert J. Wood[1,2]*

From millimeter-scale insects to meter-scale vertebrates, several animal species exhibit multimodal locomotive capabilities in aerial and aquatic environments. To develop robots capable of hybrid aerial and aquatic locomotion, we require versatile propulsive strategies that reconcile the different physical constraints of airborne and aquatic environments. Furthermore, transitioning between aerial and aquatic environments poses substantial challenges at the scale of microrobots, where interfacial surface tension can be substantial relative to the weight and forces produced by the animal/robot. We report the design and operation of an insect-scale robot capable of flying, swimming, and transitioning between air and water. This 175-milligram robot uses a multimodal flapping strategy to efficiently locomote in both fluids. Once the robot swims to the water surface, lightweight electrolytic plates produce oxyhydrogen from the surrounding water that is collected by a buoyancy chamber. Increased buoyancy force from this electrochemical reaction gradually pushes the wings out of the water while the robot maintains upright stability by exploiting surface tension. A sparker ignites the oxyhydrogen, and the robot impulsively takes off from the water surface. This work analyzes the dynamics of flapping locomotion in an aquatic environment, identifies the challenges and benefits of surface tension effects on microrobots, and further develops a suite of new mesoscale devices that culminate in a hybrid, aerial-aquatic microrobot.

INTRODUCTION

A few animal species (*1*–*5*) demonstrate the remarkable capability of hybrid aerial-aquatic locomotion to search for food sources, chase prey, and evade predators. Hybrid aerial-aquatic robots capable of traversing complex multiphase environments will have a wide range of applications, such as environmental exploration and search and rescue missions (*6*). Owing to smaller physical size and weight, microrobots are advantageous for navigating within confined and cluttered environments. Because of diminishing inertial forces at the millimeter scale, microrobots are more resilient to impact events such as a crash landing on water or collision with obstacles (*7*). Compared with conventional robots, microrobots can easily land on vertical surfaces (*8*) or even perch on overhangs (*9*) by exploiting surface effects. Despite these functional advantages, hybrid aerial-aquatic microrobots face unique fabrication challenges and physical constraints.

A hybrid aerial-aquatic microrobot must solve two key problems: (i) multiphase propulsion for air and water and (ii) overcoming surface tension for water entry and exit. The large density difference between air and water imposes conflicting criteria for robot locomotion and structural design in these two environments. A number of robotic platforms, such as fixed wing (*10*), foldable wing (*11*), and rotorcraft vehicles (*12*), have been developed to explore multiphase locomotion. Although there are no fixed wing or foldable wing designs that are fully operational in aerial and aquatic environments, a recent study adapted a rotorcraft to aquatic locomotion and further demonstrated air-to-water and water-to-air transition (*12*). However, a rotorcraft design cannot be easily adapted by a microrobot because of fabrication difficulty and surface tension effects, which can exceed robot weight by over 10 times. In addition, the physics of scaling indicates that conventional brushless motors are not feasible on the order of milligrams.

In the past decade, there has been a growing interest in studying flapping-wing flight (*13*) and developing flapping-wing robots (*14*). Aerial flapping-wing propulsion generates large lift forces by using unsteady aerodynamic mechanisms such as rotational circulation (*15*) and periodic vortex shedding (*13*, *16*). Recently, flapping aquatic locomotion was observed in zooplankton (*17*) in a similar Reynolds number regime (~100). A previous work (*18*) compared the fluid mechanical similarities of a single flapping wing in air and in water and demonstrated aerial-aquatic locomotion on an existing micro aerial vehicle. However, the work did not identify the trade-off between aerial and aquatic flapping, and consequently, the robot suffered short actuator lifetime because of stress induced by a nonoptimal choice of operation frequency.

Furthermore, surface tension far exceeds a robot's weight and its maximum lift capability at the milligram and millimeter scales. Hence, transitioning into or out of water requires novel mechanisms to overcome this effect. However, any additional mechanisms must satisfy the microrobot's subgram payload capability. This design challenge requires fabrication of lightweight, energy-efficient, and multifunctional components for locomotion and water-to-air transition. Water-to-air transition with a microrobot has not been previously demonstrated because of the difficulty in developing an impulsive mechanism that weighs less than 50 mg and operates underwater. A recent work developed a single-use chemical reaction–based thruster (*11*) that weighs 2.6 g, which is too heavy to be incorporated onto insect-scale robots. Another study used a shape memory alloy (*19*) actuator to impulsively push off the water surface for the takeoff of a 68-mg robot. However, this device cannot demonstrate repeatable takeoff, and it cannot be adapted to vehicles that are submerged in water.

[1]John A. Paulson School of Engineering and Applied Sciences, Harvard University, Cambridge, MA 02138, USA. [2]Wyss Institute for Biologically Inspired Engineering, Harvard University, Cambridge, MA 02138, USA. [3]Aerial Robotics Laboratory, Department of Aeronautics, Imperial College London, London, UK. [4]Department of Mechanical and Aerospace Engineering, University of California, San Diego, San Diego, CA 92093, USA. [5]Department of Mechanical and Biomedical Engineering, City University of Hong Kong, Hong Kong SAR, China.
*Corresponding author. Email: rjwood@eecs.harvard.edu (R.J.W.); yufengchen@seas.harvard.edu (Y.C.)

This paper identifies and resolves key challenges to achieving hybrid aerial-aquatic locomotion in a subgram microrobot. We investigated the system dynamics of aquatic locomotion and found that an intrinsically unstable aerial flapping-wing vehicle can become passively stabilized during swimming when operated at appropriate frequencies. We also developed a 40-mg impulsive device that uses electrolysis and combustion to achieve repeatable water-to-air transitions. These studies culminated in a bioinspired, flapping-wing, hybrid aerial-aquatic microrobot. Our robot successfully demonstrated aerial hovering, air-water transition, swimming, water surface takeoff, and landing (movies S1 to S4). This multifunctional microrobot is able to adapt to complex environments, and such locomotive abilities will extend the functionalities and applications of future microrobots.

RESULTS

Robot design and demonstration

To achieve efficient multimodal locomotion, the robot uses a flapping-wing design, and the motion is driven by a pair of piezoelectric actuators. We based the robot design on previous work (*14*) and modified the robot's structure with a number of micromechanical features specifically for water-to-air transition. Compared with the original robot (Fig. 1A), this design is split into two symmetric halves (Fig. 1B), leaving a large central volume to accommodate functional components for water surface takeoff. These components consist of four balance beams and small buoyant outriggers (Fig. 1, C and D), a gas collection chamber (Fig. 1, C, E, and F), and a lightweight device (Fig. 1G) that integrates electrolytic plates and a sparker (Fig. 1H). The electrolytic plates and the sparker used electrolysis reactions to achieve water surface takeoff: $2H_2O$ (l) + energy ↔ $2H_2$ (g) + O_2 (g). The interdigitated electrolytic plates (Fig. 1G) decomposed water to hydrogen and oxygen, and the sparker ignited the gas for takeoff. (A discussion on material choice and electrolytic efficiency is available in text S1 and fig. S1.) The sparker electrodes (Fig. 1H) were laser-machined to achieve a small separation gap of 20 μm, which ensured the sparking potential to be within the robot's 300-V operating voltage. The entire device was affixed vertically to the bottom of the gas collection chamber (Fig. 1E). The chamber's titanium top plate was patterned with an array of 34-μm-radius micro-openings (Fig. 1F). (The functionalities of these micro-openings are detailed in Discussion and Materials and Methods.) Four titanium T-beams (Fig. 1G) were affixed to the connections struts (Fig. 1H) above the chamber top plate to maintain robot stability on the water surface. A sealed box attached to the tip of each balance beam and functioned as a buoyant outrigger to increase buoyancy and improve underwater stability. The additional components weighed 70 mg. To carry this additional payload, we redesigned the robot transmission, flexure stiffness, and wing size such that the maximum robot lift is increased from 140 to 220 mg. The components were manufactured using the smart composite manufacturing process (*20*). (A detailed description of robot fabrication is available in Materials and Methods and table S1. The functionalities of the robot components are detailed in texts S1 to S4.)

This robot demonstrated aerial hovering, air-to-water transition, swimming, water surface takeoff, and landing (Fig. 2A and movies S1 to S4). The robot hovered in air and was intrinsically unstable without feedback. We used a motion-tracking system with adaptive control (*8*) to obtain stable hovering flight (Fig. 2B). The control signals were computed off-board and sent to the robot through a wire tether. When the robot descended onto the water surface, it broke surface tension upon impact and subsequently sunk into the aquatic environment (Fig. 2C). To hold position or maneuver once underwater, the robot flapped its

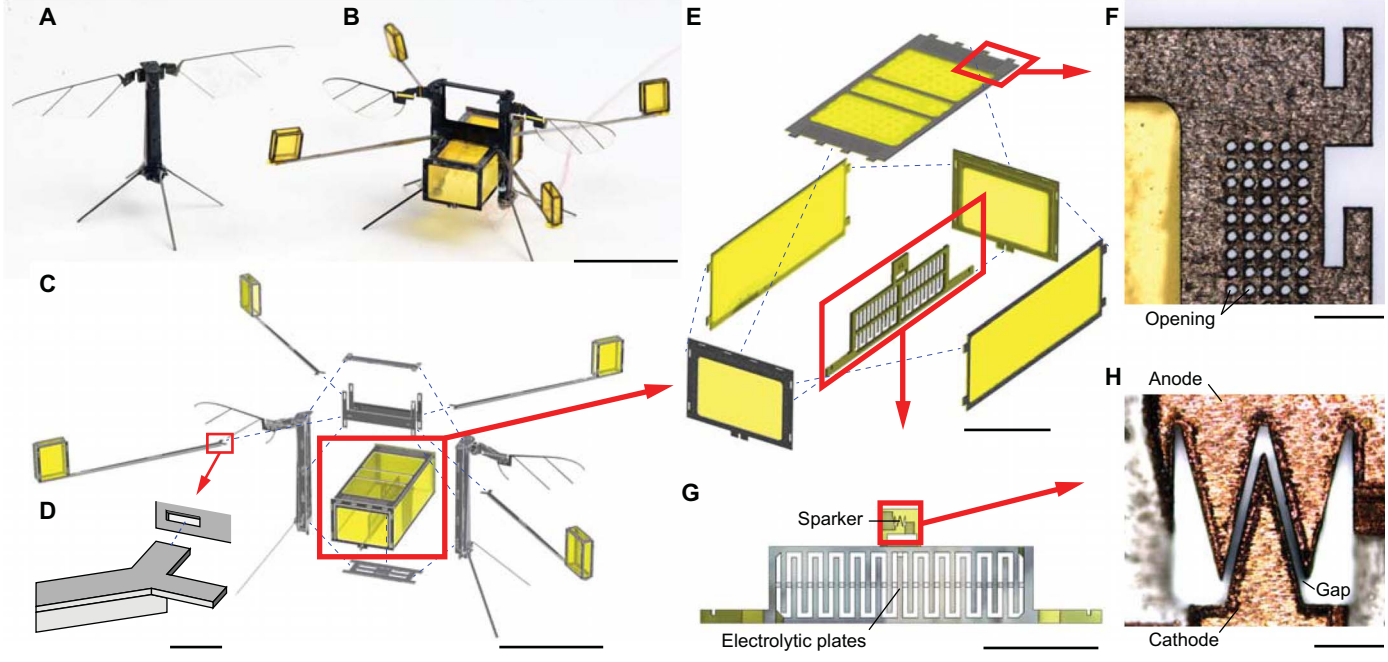

Fig. 1. Robot design, component fabrication, and assembly. (**A**) An existing 85-mg robot was used to investigate underwater stability. (**B**) The improved 175-mg robot consisted of two symmetric halves, a central gas collection chamber with a sparker plate, four balance beams, and buoyant outriggers. (**C**) Exploded view of robot assembly. Scale bar, 1 cm (B and C). (**D**) Mating feature of the titanium balance T-beam. Scale bar, 500 μm. (**E**) Exploded view of gas collection chamber assembly. Scale bar, 5 mm. (**F**) Microscopic image illustrating an array of porous openings on the chamber's titanium top plate. Scale bar, 500 μm. (**G**) The sparking plate consists of a pair of stainless steel plates and a copper sparker. Scale bar, 4 mm. (**H**) Microscopic image of the sparker electrodes. Scale bar, 100 μm.

wings at 9 Hz. When the robot began to transition out of water, it first swam up toward the surface (Fig. 2D). Upon reaching the water surface, a pair of electrolytic plates in the robot body began decomposing water into oxyhydrogen. The gas was collected by a chamber, and the increased buoyant force gradually pushed the robot's wings out of water (Fig. 2E). Last, to completely break free from the water surface, we used an impulsive strategy: A sparker ignited the oxyhydrogen mixture, and the robot jumped off the water surface (Fig. 2F). This combustion-based takeoff resulted in a typical takeoff velocity of 2.5 m/s and a typical jump height of 37 cm (Fig. 2F and movie S4). The robot assumed a ballistic trajectory in air and landed on the ground about 0.55 s after takeoff. Because of spatial constraints of the motion capture arena and potential adverse effects of oxyhydrogen combustion on sensitive tracking instruments, open-loop demonstrations of air-to-water transition, swimming, and water-to-air transitions were performed in a separate setup. In the following sections, we present detailed results on robot aquatic locomotion and transition between aerial and aquatic environments.

Aquatic locomotion and passive swimming stability

To reconcile the density difference between air and water, the robot operating frequency in aquatic environments needed to be lowered according to the scaling relationship outlined in a previous work (*21*). The reduction of flapping frequency led to stronger body-wing coupling and caused larger damping on the robot body, which strongly influenced the robot swimming stability. We developed a dynamical model, conducted robot swimming experiments to investigate the robot body-wing coupling, and found that the robot becomes passively stabilized when operated at appropriate frequencies.

The swimming simulations and experiments were based on a previous robot design (*14*), and the results were incorporated into the new robot design. The time-varying dynamical model took in robot actuator torques as the driving functions and solved for the robot center of mass position, the attitude, and the relative wing kinematics. (Model derivation is available in text S5.) In each of the simulations, we set the robot actuator driving torque to a sinusoid with an amplitude of 15 μNm and let the simulations run open-loop for eight flapping periods. These simulations aimed to investigate the influence of varying flapping frequency on swimming stability.

The previous robot design operated at 140 Hz in air, and a scaling relation (*18*) estimated a 5-Hz flapping frequency in water. When the flapping frequency was set to 5 Hz, the simulation showed that the robot was unstable. The robot became stable when the flapping frequency was increased to 11 Hz (Fig. 3, A to C). Figure 3A shows the trajectory and velocity of the body center of mass. The color scale represents the instantaneous speed. This simulated trajectory is qualitatively similar to the swimming motion of sea snails (*17*). Figure 3B shows the body center of mass velocity as a function of time. The body ascending speed is sinusoidal with a mean of 80 mm/s and an amplitude of 15 mm/s. Figure 3C shows body rotation. The body pitch motion is approximately sinusoidal with an amplitude of 9.3°. Because the flapping kinematics of the two wings are symmetric, there is no rotation along the roll or yaw axes. (Definitions of robot roll, pitch, and yaw axes are given in text S5.)

To validate the model prediction, we conducted swimming experiments at different frequencies using the previous design. When flapping at 5 Hz, the robot experienced large body pitching and plunged downward within 2 s after takeoff from a horizontal platform under

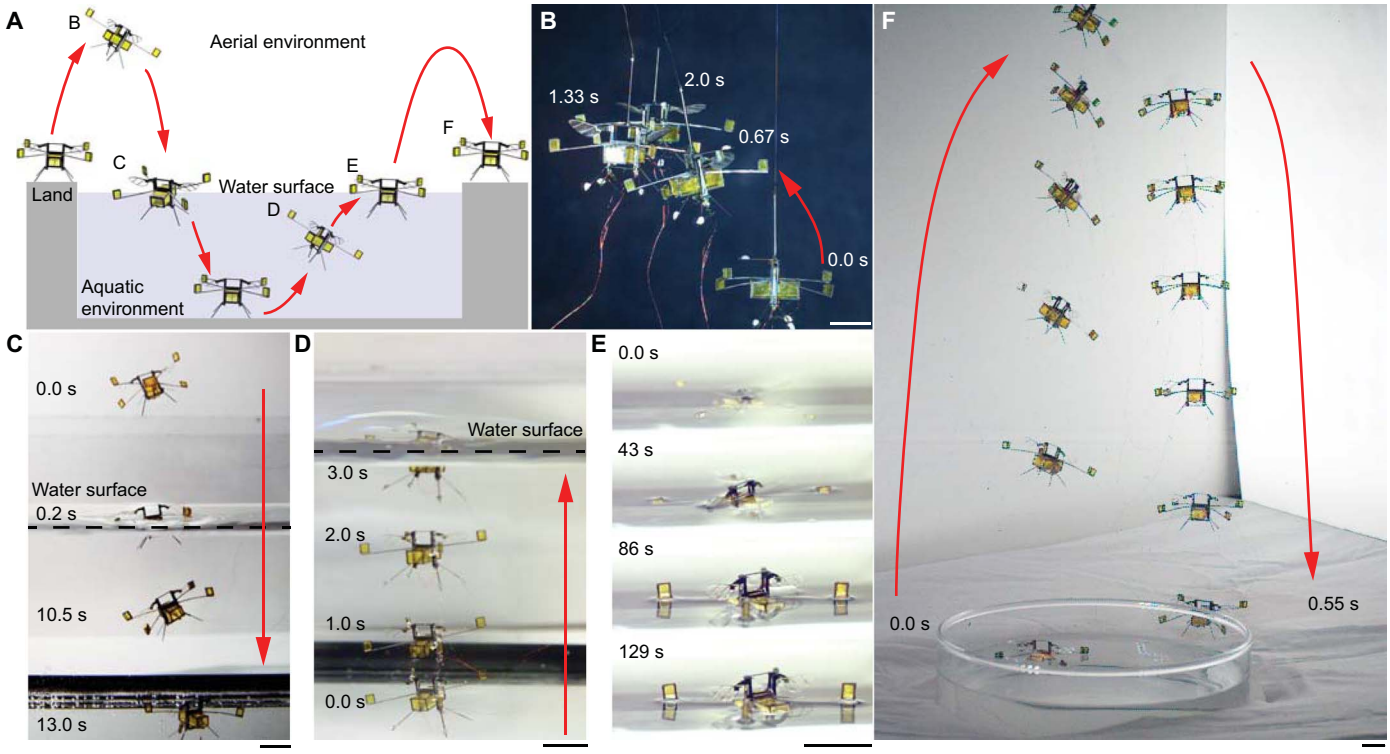

Fig. 2. Demonstration of aerial-aquatic locomotion and transition. (**A**) The robot is capable of aerial hovering, air-to-water transition, swimming, water-to-air transition, impulsive takeoff, and landing. (**B**) Composite image of a hovering robot. (**C**) Composite image of the robot transitioning from air to water. (**D**) Composite image of the robot swimming to the water surface. (**E**) Images of the robot gradually emerge from the water surface by capturing gas from electrolysis. (**F**) Composite image of robot takeoff and landing. Scale bars, 1 cm.

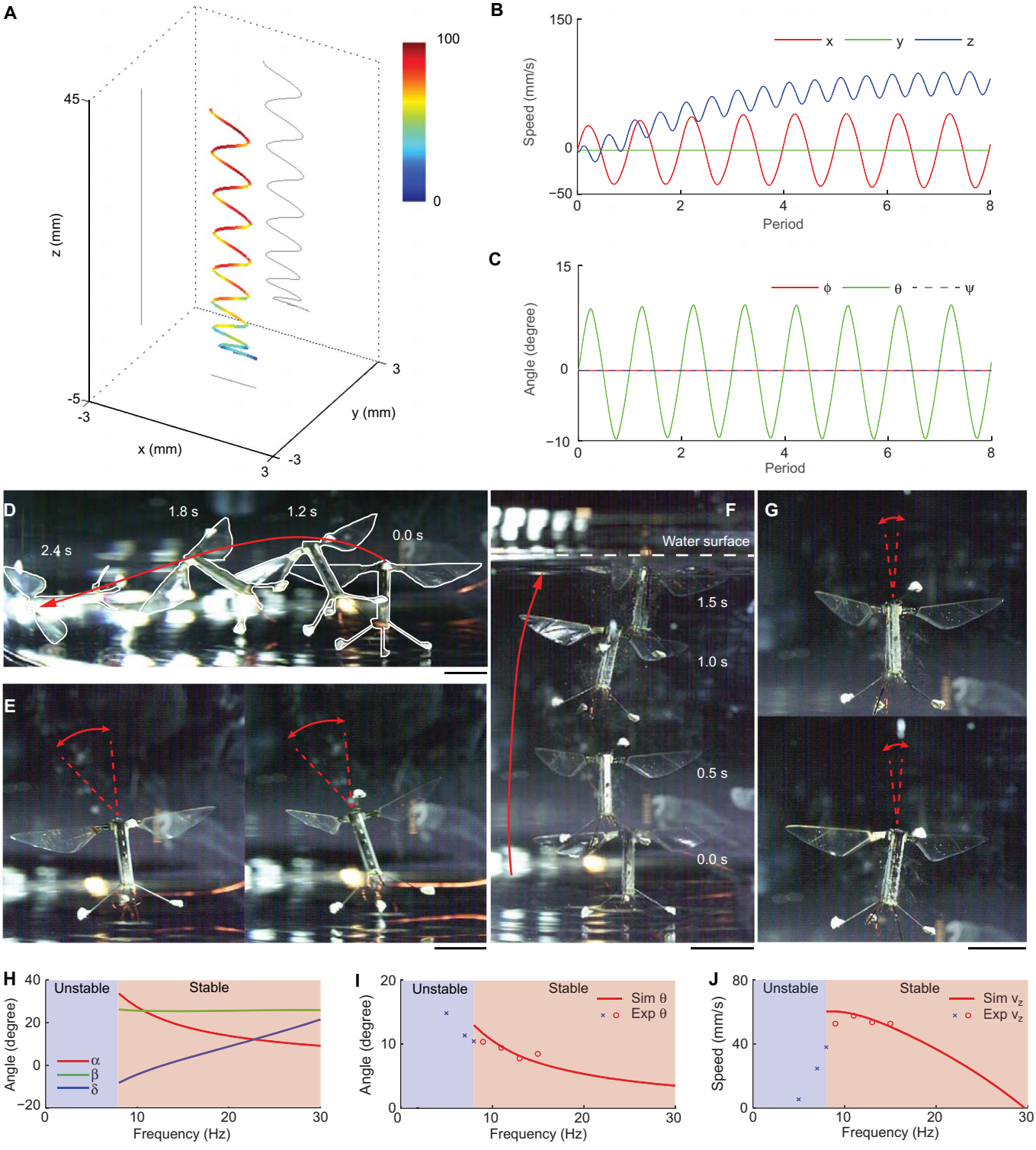

Fig. 3. Simulations and experiments of robot swimming stability. (**A**) Simulation of the robot center of mass motion when it is driven at 11 Hz. The color scale represents vehicle speed and has units of millimeter per second. The flapping frequency is 11 Hz. (**B**) Robot center of mass velocity. (**C**) Robot body rotation. ϕ, θ, and ψ represent the body yaw, pitch, and roll motion, respectively. (A to C) Results of the same simulation. (**D**) Composite image of an unstable swimming robot operating at 5 Hz. (**E**) This robot experiences notable body pitching (14.8°) when it flaps wings at 5 Hz. (**F**) Composite image of an upright stable robot ascending to the water surface. (**G**) The robot pitching amplitude reduces to 9.4° when swimming frequency increases to 11 Hz. Scale bars, 1 cm (D to G). (**H**) Simulation results of wing stroke (α) and pitch (β) amplitude and relative phase (δ) as functions of flapping frequency. (**I**) Experimental and simulation comparison of robot pitch amplitude as a function of flapping frequency. (**J**) Experimental and simulation comparison of robot ascent speed as a function of flapping frequency. (H to J) Red and blue colors distinguish regions that are either stable or unstable, respectively. Both experiments and simulations show that the robot is unstable when the flapping frequency is lower than 9 Hz.

water (Fig. 3, D and E, and movie S5). When flapping frequency increased to 11 Hz, the robot ascended to the water surface (Fig. 3F), and its body pitch amplitude reduced notably (Fig. 3G). This observation supports the model prediction. To quantify the robot body oscillation, we extracted the body kinematics from the recorded videos. (Details and examples of the tracking method can be found in text S6.)

To explore the influence of flapping frequency on robot swimming stability, we repeated the simulations with frequencies in the range of 1 to 30 Hz. Figure 3 (H to J) shows robot pitching and ascending speed as functions of frequency. The definition of pitch stability is given in text S7. A simulation terminates if the robot state violates the stability conditions, and the corresponding frequency is colored blue. If the simulation satisfies the stability conditions, then the corresponding frequency is colored red. Figure 3H illustrates the wing stroke and pitch kinematics. (The definition and illustration of wing stroke, pitch, and phase shift are available in text S5.) The red curve shows that the wing stroke amplitude reduced as the frequency increased. The green curve shows that the wing pitching remained nearly constant. The blue curve shows that the relative phase shift increased as driving frequency increased. The effects of frequency increase and stroke amplitude decrease on lift production approximately cancel each other out. The increase in phase shift implies that the lift force is reduced at high flapping frequencies (*16*).

Body pitching and robot ascending speed are decreasing functions of frequency (Fig. 3, I and J). These simulations show that there are two competing effects influencing robot aquatic locomotion. At low flapping frequencies, large body rotations destabilize the vehicle; at high frequencies, large phase shifts between the wing stroke and pitch kinematics reduce lift. These simulations show that the robot becomes stable at high frequencies, but the mean lift force and maximum ascending speed decrease (Fig. 3J) due to unfavorable flapping kinematics. To corroborate the simulation results, we conducted experiments by driving the previous robot design in the range of 5 to 15 Hz. In these experiments, the robot's actuators failed at frequencies greater than 15 Hz (due to excess stress on the piezoceramic caused by the increased loading). Our simulation results agree well with experimental measurements of the maximum ascending speed, body pitch amplitude, and stability conditions (Fig. 3, I and J, and movie S6). In summary, the robot becomes passively upright stable at appropriate frequencies due to damping on the robot body and body-wing coupling. For the previous robot design, the lowest stable swimming frequency is almost twice that of the system resonance (resonance refers to the frequency corresponding to the largest wing stroke motion). As a consequence of driving the actuator beyond the resonant frequency, the actuator lifetime is severely reduced. The phase difference between the actuator tip motion and the wing flapping motion grows markedly beyond resonance. As a consequence, the actuator experiences large stress, and this leads to cracking of the actuators. In the new robot design, we aimed to ensure robot swimming stability at the system resonant frequency. These experiments and simulations offer important guidelines for the new vehicle design. Achieving passive stability during swimming is important for our experiments because the current infrared-based motion-tracking system does not operate in water due to refraction. Consequently, all swimming experiments were conducted open-loop without feedback control, and the robot must maintain passive stability. For future aquatic flapping-wing robots that are equipped with attitude and position feedback, achieving passive stability is still beneficial to reduce the cost of sensing and control.

Our simulation and experimental results suggest that the appropriate swimming frequencies are in the range of 9 to 13 Hz. To achieve such flapping frequency in water, the robot aerial flapping frequency needs to be increased to 220 to 300 Hz. On the basis of a scaling relation between frequencies and wing size (*21*), we reduced wing area by 40% to accommodate the required increase of flapping frequency. In addition, the simulation further suggests that robot body pitching can be reduced by increasing moment of inertia along the pitch axis and lowering the body center of mass. These findings were incorporated into the new vehicle design to improve stability and water-to-air transition capability. The gas collection chamber and sparking plates were placed below the robot center of mass; the frontal area served to increase body damping, and the distribution of mass away from the pitch axis increased the pitch inertia.

We conducted swimming experiments using the new robot design to demonstrate vehicle stability. In accordance with our prediction, the resonant frequency was measured to be about 9 Hz. Figure S2A demonstrates that the robot swam stably toward the water surface at 20 mm/s. The robot sank passively to the aquarium bottom when it was switched off. Figure S2B further shows that at the resonant frequency, the robot experienced small body pitching, which is notably smaller than that of the old design (Fig. 3E). Unlike the previous robot design, which suffered from short actuator lifetime due to operating at twice the robot resonant frequency in water, the new design was able to maintain upright stability when operating at its resonant frequency in water. We further conducted swimming experiments by varying the driving frequency from 7 to 11 Hz. The robot swims stably to the water surface for frequencies larger than 7 Hz. At 7 Hz, the robot is unable to lift off due to insufficient lift. In the following sections, all simulations, measurements, and experiments were done using the improved robot design to investigate air-to-water and water-to-air transitions.

Surface tension effects on air-to-water and water-to-air transitions

Surface tension imposes extreme difficulties on air-water transitions for mobile objects at the millimeter scale. Whereas impact forces from large diving objects (*22*–*24*) can easily break the water surface, water entry for millimeter-scale objects is difficult because surface tension is comparable with vehicle weight. To take off from the water surface, the robot must overcome surface tension and gravity while maintaining upright stability. We quantified the surface tension effects on our robot and proposed strategies for air-to-water and water-to-air transitions.

To quantify the surface tension effect on water entry and takeoff, we mounted the robot on a capacitive force sensor (Fig. 4A). The robot was lowered into or pulled out of water at a constant speed of 0.2 mm/s. We conducted experiments using either soapy water or tap water and quantified the effects of the surfactant. Instead of coating the robot with surfactant, we put three to five drops of Joy liquid detergent in about 200 ml of tap water.

First, we lowered a robot that was completely dry into soapy water and measured the corresponding forces (Fig. 4B). The robot experienced an upward buoyant force as it was lowered into water. In addition, deformation of the water surface caused an upward surface tension force during water entry. The net buoyant force is given by the sum of contributions from the robot body, the sealed buoyant chambers, and the air trapped in the gas collection chamber:

$$F_{\text{bouy}} = F_{\text{b,robot}} + 4\rho_{\text{w}} g V_{\text{c}} + \rho_{\text{w}} g V_{\text{g}} \quad (1)$$

In this equation, ρ_{w} is the water density, V_{c} is the small chamber volume, and V_{g} is the volume of trapped air. Without any trapped air

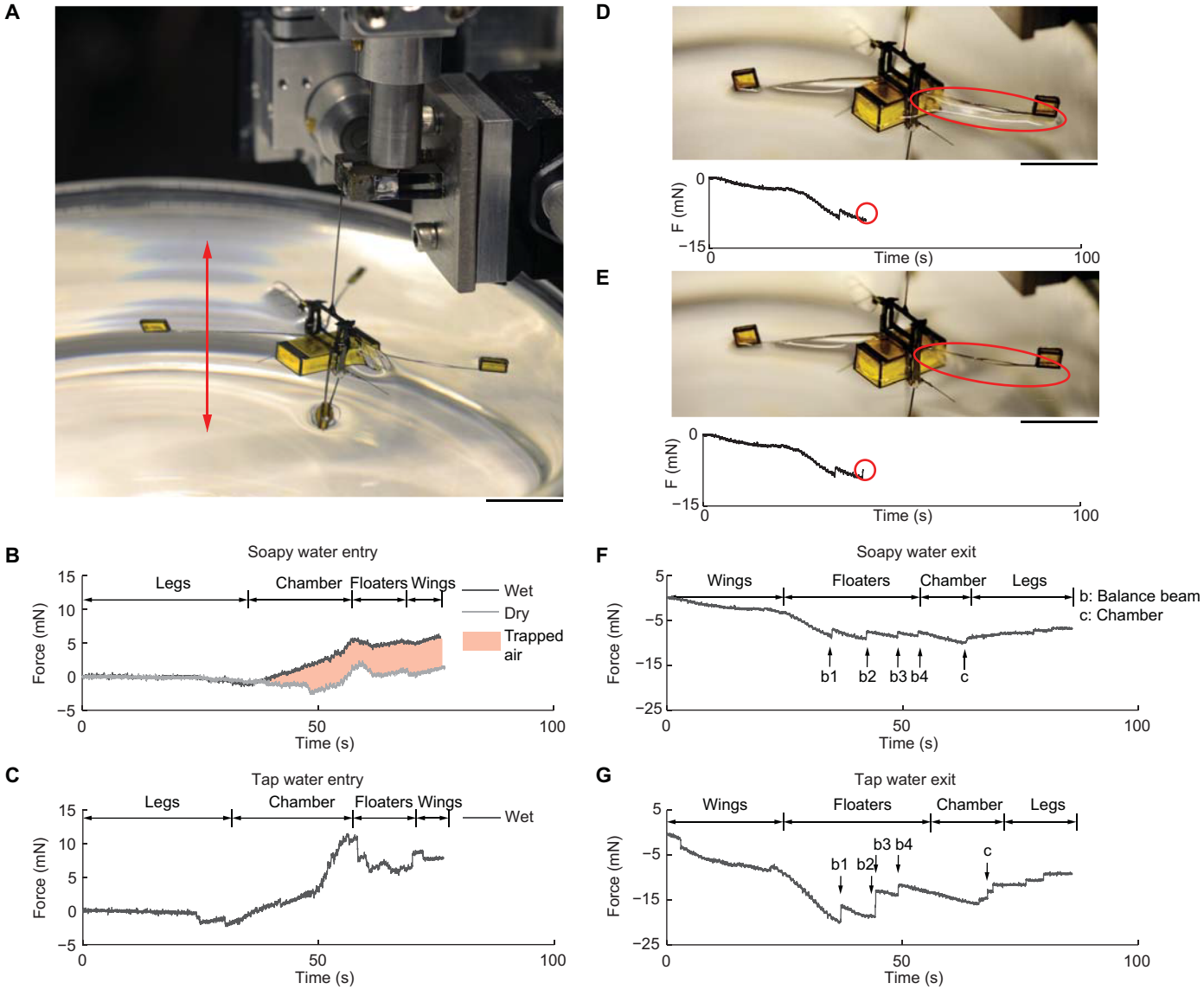

Fig. 4. Robot surface tension experiments. (**A**) Illustration of the experimental setup. The robot is mounted on a capacitive force sensor and is slowly lowered into water or pulled out of water. (**B**) Force trace when the robot is lowered into soapy water. (**C**) Force trace as the robot is lowered into tap water. (**D**) Picture of the robot and force trace immediately before one of its balance beams (red circle) pops out of the water surface. (**E**) Picture of the robot and force trace immediately after one of its balance beams (red circle) pops out of the water surface. (D) and (E) are taken 0.33 s apart. (**F**) Force trace as the robot is pulled out of soapy water. (**G**) Force trace as the robot is pulled out of tap water. Scale bars, 1 cm (A, D, and E).

($V_g = 0$), the net buoyancy force was estimated to be about 1.1 mN. For the case of lowering a dry robot into soapy water, we measured the maximum force of 1.8 mN. The net force after the robot fully submerged is 1.3 mN, which implies that 20 mm^3 of air is trapped in the gas chamber or the robot body.

The experiment was repeated with a wetted robot (Fig. 4B). A thin film of water covered the micro-openings and trapped air during water entry. The maximum measured force was 6 mN, which implies that 490 mm^3 of air was trapped in the gas chamber or the robot body. The red colored region in Fig. 4B shows the amount of captured gas due to covering of the micro-openings. Next, we lowered a wetted robot into tap water and observed a substantial increase in surface tension. The maximum force for tap water entry is 11 mN (Fig. 4C). The net buoyancy force on trapped air, small buoyant outriggers, and the robot body sum to 7.6 mN, which implies that surface tension is about 3.4 mN in tap water. These experiments suggest that the micro-openings are necessary to reduce trapped air and enable water entry. The Bond number—the ratio of the robot weight to surface tension—is a convenient metric to assess whether the robot will penetrate the water surface or not. Without a surfactant (soap), the Bond number is 0.7, which prohibits direct air-to-water transition. With the addition of soap, the Bond number increases to 2, which indicates that direct transition is possible.

To demonstrate water entry, we coated the robot balance beams and air frame with surfactant and conducted a number of freefall tests under different heights (movie S2) and configurations (fig. S3). Movie S2 shows that the robot can break the water surface when it falls from

between 2 and 10 cm above the water surface. Without applying surfactant, the robot cannot break the water surface. Figure S3 shows successful robot water entry when it lands from different orientations.

Next, we measured the forces on the robot as it was pulled out of water. As the balance beams emerged from the water surface, a thin water film formed and stretched to the free surface (red circled region of Fig. 4D). This thin film collapsed as the robot continued to rise, and consequently each balance beam popped out of the water (Fig. 4E). This motion is captured by the discontinuities in the force plots (Fig. 4, D to G, and movie S7). The magnitudes of these discontinuities quantified the surface tension forces on the balance beams and the chamber. In soapy water, the corresponding forces were 1.3 and 1.4 mN (Fig. 4F). We repeated the experiment in tap water (Fig. 4G) and measured 3.6- and 4.4-mN force on balance beam and chamber, respectively.

We modeled the surface tension forces using the formula (*25*) $F_s \approx 2\gamma L$, where γ is the surface tension coefficient and L is the wetted length. This equation assumes that the floating object is a one-dimensional thin wire. In soapy water, we estimated the surface tension forces on a balance beam and the chamber to be 1.2 and 2.0 mN, respectively. In tap water, the forces increase to 3.6 and 6.0 mN due to a larger γ. The estimates agree well with balance beam measurements but overpredict the force on the chamber. The discrepancy is largely contributed by the chamber corners because they do not satisfy the one-dimensional assumption.

The robot has four balance beams and one gas collection chamber. In soapy water and tap water, the total surface forces on these components are 6.6 and 18.8 mN, respectively. This result suggests that direct liftoff from the water surface is infeasible, because a previous work (*26*) reports a maximum lift of 3.1 mN. In the next section, we describe energetic impulsive mechanisms that enable the water-to-air transition.

Water-to-air transition strategy

To achieve a water-to-air transition, our robot uses a two-step process: gradual surfacing of its wings followed by impulsive takeoff. Upon reaching the water surface, the electrolytic plates convert water into oxyhydrogen. Although the gas collection chamber has micro-openings on its top plate, it can still capture the produced gas through surface tension effects. (An extended discussion on micro-opening radius influence on gas collection is given in text S2 and fig. S4.) The gradually increasing buoyant force of the system gently pushes the robot's wings out of the water. In this process, surface tension on the balance beams maintains the robot's upright stability (see text S2 and fig. S5, E and F). This approach protects the delicate wings and transmission from high drag forces experienced upon impulsive transition to air. The second step generates an impulse that breaks the water surface. Previously developed impulsive takeoff methods involved either a fast push off from the water surface (*19*, *27*) or chemical reaction–based jet propulsion (*11*). Because of limited payload, our robot requires a novel method for repeatable takeoff. Here, the robot uses reverse electrolysis to acquire energy for takeoff. Compared with other chemical-based propulsion, this method is repeatable and has benign reaction by-products.

The robot prepares for impulsive takeoff after its wings completely emerge from the water. At this time, the gas chamber is filled with oxyhydrogen that contains sufficient energy to break the water surface. The robot switches off its electrolytic plates and briefly flaps its wings to remove water residue. Next, a 250-V pulsed signal (Fig. 5A) is sent to the sparker plate, and corona discharge is generated within the 20-μm gap between the sparker plate electrodes. We found that the ignition energy is about 0.2 mJ by measuring the corresponding current and pulse duration (Fig. 5A). The detonation of oxyhydrogen (*28*) immediately increased pressure within the gas chamber (Fig. 5B). This detonation completed within 1 ms, broke the water surface, and exerted an upward impulse on the robot. The average upward force generated within the first millisecond was between 7.5 and 9 N, resulting in a device thrust-to-weight ratio of 19,000 to 23,000. Without the micro-openings, excessive detonation pressure damaged the chamber, balance beams, and robot wings (Fig. 5C). The robot without micro-openings took off at 3.4 m/s and experienced large body rotation (Fig. 5D). In contrast, the presence of micro-openings reduced maximum pressure by 3.4 times and widened the initial pressure pulse width by 39% (Fig. 5B), thereby minimizing structural damage. The chamber with micro-openings experienced a smaller pressure rise (Fig. 5B) by releasing gas through its openings (Fig. 5C). These micro-openings further reduced the robot's takeoff speed and body rotation (fig. S6, D and E). With the micro-openings, the robot took off at 1.8 m/s and the robot was undamaged. The balance beams stabilized the takeoff via surface tension and viscous shear. Consequently, the robot experienced only small body rotation during takeoff (Fig. 5D and movie S8). (An extended discussion of the micro-opening influence on takeoff is available in text S4 and figs. S6 and S7.)

Robot landing and post-takeoff flight

Because of motion-tracking limitations, we cannot implement feedback control for impulsive water surface takeoff. The current Vicon motion-tracking system uses infrared strobe illumination to capture the motion of reflective markers attached to the robot. This system needs to operate in a dark arena without reflective surfaces. Water refracts infrared radiation and creates very large tracking noise, making optical tracking infeasible. Instead, the robot passively lands after takeoff (Fig. 2F). By extracting images from movie S4, we measured the maximum jump height to be 37 cm.

We defined a successful landing as the case when the robot lands upright on a surface. The probability of successful landing is dependent on the landing surface. We dropped the robot from 35 cm above different surfaces and repeated the experiment 10 times. On pretensioned nylon cloth, the robot successfully landed 60% of the time. However, the success rate dropped to 10% on stainless steel surfaces. These results show that landing success rate is substantially higher on elastic surfaces. Pretensioned nylon cloth absorbed the landing impact, and there was very small subsequent bounce. The bounce magnitude notably increased on rigid steel surfaces and reduced the landing success rate. This experiment suggests that future robot designs may benefit from introducing compliance to the landing legs or from designs that passively orient the robot while on land.

To verify system repeatability, we conducted a number of static tests and flight experiments after impulsive takeoff and landing. In most experiments, the robot experienced no visual damage after transitioning from water to land. (Detailed statistics of impulsive takeoff are given in text S4.) The robot was dried naturally, and it was first tested statically without any mechanical modification after the explosion. Figure S8 compares the flapping kinematics of the robot operating at 265 Hz before and after impulsive takeoff. The robot left and right wing stroke amplitudes before explosion were measured to be 37.5° and 36°, respectively. The robot left and right wing stroke amplitudes after explosion were measured to be 40° and 36°, respectively. This comparison shows that the robot can generate similar flapping kinematics, which implies that its lift capability remains similar.

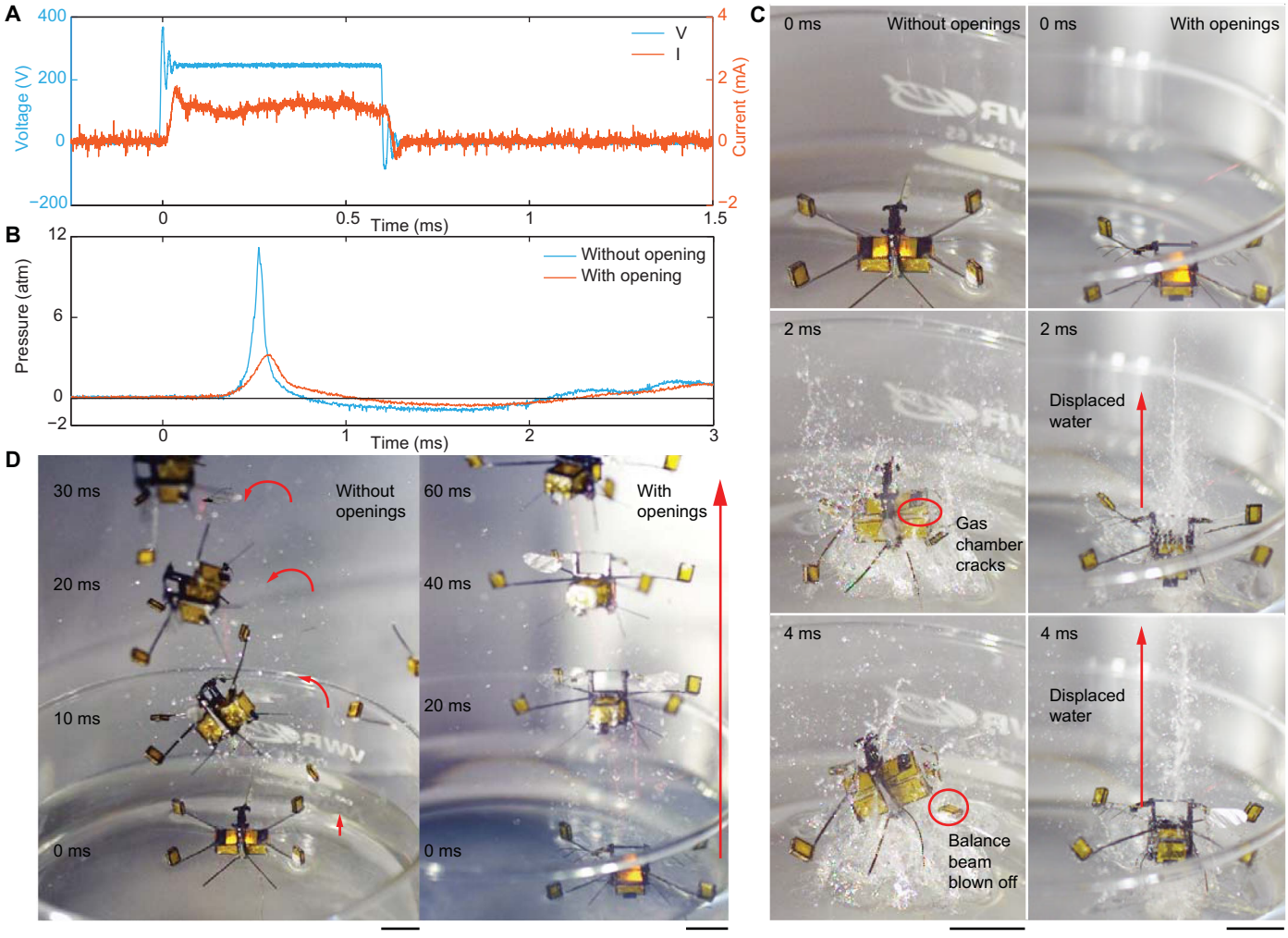

Fig. 5. Impulsive takeoff from the water surface. (**A**) Sparker plate input voltage and current when a visible spark is generated. (**B**) Pressure profile within the chamber upon oxyhydrogen ignition. A reinforced chamber without micro-openings experiences higher pressure than one with micro-openings. (**C**) Image sequence comparison of initial robot takeoff. For the robot without chamber micro-openings (left), the detonation cracks the chamber top plate and detaches a robot balance beam and wing. For the chamber with micro-openings (right), gas and water are released upon ignition, and the robot remains undamaged. (**D**) Overlaid image comparison of robot takeoff. A robot without chamber micro-openings experiences substantial body rotation and has a higher takeoff speed (left). A robot with chamber micro-openings maintains upright stability and has lower takeoff speed (right). Scale bars, 1 cm.

Furthermore, we show that the robot is capable of demonstrating open-loop takeoff after explosion. Figure S9 compares the takeoff demonstration of the robot before and after explosion. For open-loop takeoff, we only turn on the robot for 0.3 s (~100 flapping periods), because without control the robot may experience large body rotation and its wings may collide with the safety tether. After explosion, the robot can still lift off with an average acceleration of 20 cm/s^2. This implies that the robot can generate a mean lift force larger than its weight after the impulsive takeoff.

To achieve similar hovering performance, we performed additional wing hinge pairing, open-loop trimming, and closed-loop control parameter identification, because the explosion created small changes to the robot structure. This tuning process was only required for hovering flight and was a regular procedure that was frequently done between flight trials. Details of the tuning procedure are given in Materials and Methods. For cases that involve small visual damages (e.g., lost of a leg or a buoyant outrigger), the robot is also capable of hovering after affixing the component and tuning. This implies that the impulsive takeoff does not cause critical damage to the robot's main structure or actuators. However, it creates small changes to the operating condition such that tuning is needed to demonstrate hovering. Tuning the operating condition is something that could in the future be achieved autonomously through either adaptive control or iterative learning techniques.

DISCUSSION

Our presentation of a hybrid aerial-aquatic, flapping-wing microrobot includes (i) a detailed analysis of the observation on robot passive upright swimming stability in water, (ii) the challenges and benefits imposed by water surface tension on millimeter-scale robots, (iii) a discussion of mesoscale device design, and (iv) an impulsive water-to-air transition method. The observation that a flapping-wing vehicle can be passively stabilized in water can be generalized to larger, traditional

robots. Flapping-wing locomotion in aerial and aquatic environments does not place constraints on vehicle size and weight. Flapping-wing design has a number of favorable features over traditional fixed wing and rotorcraft vehicles. For fixed wing aerial vehicles, aquatic locomotion can be inefficient because of large frictional drag on the airfoil surface. For rotorcrafts, the vehicle needs to tilt by 90° (*12*), and this configuration induces large form drag because of the large exposed frontal area. Furthermore, aerial and aquatic propellers have distinctively different shapes because of the difference in fluid properties. An aerial propeller can cause cavitation in water when it rotates at high speeds. In contrast, efficient flapping propulsion in water and air does not require changes to wing planform (*18*).

Although previous works consider surface tension and demonstrate either water surface walking (*29*) or jumping (*19*), none addressed the challenges of air-to-water and water-to-air transition at this scale. We developed a number of mesoscale devices and features that take advantage of surface tension. For instance, the balance beams use surface tension to stabilize the robot on the water surface in preparation for impulsive takeoff. The gas collection chamber uses surface tension effects to capture gas despite the presence of micro-openings on its top plate. Meanwhile, microrobots need to fight against surface tension during these transitions. Surface tension can be reduced by coating the robot with a surfactant for water entry, and it is overcome during water surface takeoff through an impulsive method. Future aquatic microrobots may use surface tension to achieve a variety of interesting applications. For instance, surface tension effects may be used to adhere to underwater surfaces or to control surface tension magnitude to either move on the water surface or transition into water.

Our multifunctional microrobot adapts to multiple environments. Traditionally, microrobots have limited functionalities because of constrained payload (*14*, *30*). To address this challenge, we developed multifunctional mesoscale devices and demonstrated multimodal locomotion strategies. For instance, the micro-openings (Fig. 1F) on the robot chamber top plate serve multiple functions. When the robot is dry, air within the chamber exits through the micro-openings, reducing buoyancy and facilitating the air-water transition. When the robot is wet, thin films of water cover the micro-openings due to surface tension. The gas collection chamber can then generate and capture gas once fully submerged in water. Upon combustion-based takeoff, these micro-openings enable excess gas pressure to escape, preventing structural damage during detonation. In addition, the multimodal locomotive strategy allows the robot to use one set of actuation to move in different environments. This robot is an example of bioinspired engineering, but it is also representative of capabilities that go beyond what nature can achieve. Although examples of insects that can perform a water-to-air transition exist (e.g., whirligig beetle family), none can do so impulsively, largely because of the power density constraints on their musculoskeletal system and the dominance of surface tension at these scales.

Next-step challenges

Our robot cannot yet demonstrate flight immediately upon impulsive takeoff because of the lack of onboard state estimation sensors and limitations in our current motion-tracking system. To enable airborne takeoff from the water surface, future studies will need to incorporate onboard sensors for fast attitude and position feedback. The current takeoff speed is about four times the maximum robot flight speed, and the robot stays aloft for 0.5 s before landing. We estimate that a motion-tracking system of comparable accuracy needs to operate around 1 kHz for attitude feedback. Furthermore, low-latency controllers need to compensate for disturbances from the impulsive takeoff, water residue, local wind gusts, etc. About 30 to 45 mg of water residue add to the vehicle payload. Although this additional payload is within the current vehicle's maximum liftoff capacity, the water residue may offset the robot center of mass and adversely affect hovering. To account for the water residue, we estimate that a future vehicle needs 30 mg of additional payload capacity and ±0.1 μNm of torque capability for pitch and roll control.

MATERIALS AND METHODS

Robot fabrication

The robot body and wings are fabricated through processes developed in a previous study (*31*). Robot actuator, transmission, and wing planform are redesigned on the basis of recent results (*26*) to increase flapping frequency and maximum lift. Each robot half weighs 45 mg. The weight of each component is detailed in table S1.

The gas chamber consists of five rectangular, planar laminates. The top piece is made from 50-μm titanium sheet laminated with 12.7-μm polyimide. It is patterned with a rectangular array (39 × 12) of circular holes with 34-μm radius. The four side pieces are made of 100-μm carbon fiber laminated with 12.7-μm polyimide. The bottom face is left open for gas collection. The chamber is assembled using tab-and-slot features to ensure precision and strength. The assembled chamber is glued using Loctite 60 Minute Epoxy. The chamber weighs 33 mg and has dimensions of 14 mm × 6.7 mm × 4.9 mm.

Each balance beam consists of two 50-μm titanium pieces. These are assembled manually to form a T-beam using tab-and-slot assembly. Each balance beam is 25 mm long, 400 μm wide, and 400 μm tall and weighs 2 mg.

Each buoyant outrigger has dimensions of 2.5 mm × 2.5 mm × 1 mm and attaches to the tip of the balance beam. The buoyant outrigger consists of three carbon fiber and polyimide laminated pieces: square top and bottom pieces and a foldable side piece. The foldable side piece is manually folded along compliant flexures. Then, the top and square pieces are assembled using tab-and-slot features. Last, the box is sealed using CA glue (Loctite 416).

The sparker plate consists of 150-μm copper clad FR-4 (glass-reinforced epoxy laminate sheet) and 25-μm stainless steel laminated layers. FR-4 provides structural support, the copper serves as a soldering pad and sparker material, and the stainless steel is used for electrolysis. The sparker plate has three functional parts: a shared ground, a low voltage plate for electrolysis, and a high voltage copper plate for generating sparks. Tether wires are soldered on copper pads, which connect to corresponding stainless steel plates via conductive epoxy. The sparker plate weighs 6.5 mg.

Copper is a favorable sparker material because of higher thermal conductivity. Figure S1 (A and B) compares new stainless steel sparker tips and shorted sparker tips. The stainless steel sparker tips fused together after three ignitions, and we observed noticeable discoloration (fig. S1B). In contrast, the copper sparker can ignite over 40 times.

In contrast, the electrolytic plates are made of stainless steel because copper anodes easily oxidize in water. Figure S1 compares new copper plates (fig. S1C) and oxidized plates (fig. S1D) after 120 s of use. Figure S1E further highlights an oxidized anode. Consequently, we chose stainless steel as the anode material. The stainless steel electrolytic plates can operate for more than 600 s without severe oxidization.

Last, all of the robot components were assembled. Four 160-μm-thick carbon fiber struts securely connected the two robot halves (Fig. 1C).

Then, four balance beams were inserted into the slots on connection pieces. Next, each buoyant outrigger was attached to a balance beam. Then, the gas collection chamber was inserted between the robot halves (Fig. 1C). The sparker plate was installed to the bottom of the gas collection chamber. Before conducting flight tests, we applied liquid surfactant (Joy liquid detergent) on the robot balance beams, airframe, and gas collection chamber using a microbrush. The robot dried naturally in 24 hours. The added mass from the surfactant was less than 1 mg, and it did not affect flight or swimming capabilities. To avoid spreading surfactant to water, future studies should consider nondissolving hydrophobic coatings.

Aerial experiment setup

We conducted the robot hovering demonstration using an existing setup (*14*). The closed-loop controller was modified from a previous study (*8*). During the hovering experiment, we attached a safety tether to the top of the robot to prevent crash landing after flight. To achieve good hovering flight, the robot needed to be mechanically tuned. This was a frequent procedure that took place between flight experiments, and the controller parameters were also updated in the process.

The mechanical tuning procedure is as follows: (i) statically flap the robot near the resonant frequency (265 Hz) to see whether system resonance slightly shifts, (ii) adjust robot wings and wing hinges for pairing (this refers to offsetting the wing attachment to account for the slight asymmetry in the left and right wings; this mechanical tuning minimizes the torque asymmetry generated by the two wings), and (iii) perform a number of open-loop flights for choosing the controller parameters (such as torque bias and mapping from input voltage signal to compensating torque amplitude).

Aquatic experiment setup

Robot swimming experiments were conducted in a 30 cm × 15 cm × 15 cm aquarium (fig. S10A). An open-loop controller commanded the flapping frequency and amplitude through the robot's tether. The robot's swimming kinematics were filmed using a Phantom v7.10 color camera. The scene was illuminated by a light-emitting diode (LED) array.

Robot takeoff and landing experiments were conducted in a beaker of radius 7.5 cm (fig. S10B). A prestretched nylon cloth was placed at the water level as the landing surface. We filmed the robot takeoff using a Phantom v7.10 color camera and a v7.3 black and white camera. The scene was illuminated by a VIC 900590P LED array. We used a Kistler 601B1 pressure sensor to measure the detonation pressure upon ignition.

SUPPLEMENTARY MATERIALS

robotics.sciencemag.org/cgi/content/full/2/11/eaao5619/DC1
Text S1. Electrolytic plate geometry and efficiency.
Text S2. Effect of micro-openings on gas capture.
Text S3. Robot stability near the water surface.
Text S4. Effect of micro-openings on takeoff.
Text S5. Derivation of dynamical model.
Text S6. Robot tracking.
Text S7. Simplified model of robot passive upright stability.
Fig. S1. Material selection of sparker and electrolytic plates, and plate geometry influence on water resistance during electrolysis.
Fig. S2. Swimming demonstration of the new robot design.
Fig. S3. Robot water entry from different orientations.
Fig. S4. Surface tension influence on height of the gas collection chamber.
Fig. S5. Robot stability near the water surface.
Fig. S6. Influence of micro-openings on takeoff speed.
Fig. S7. Influence of micro-openings on ignition pressure and takeoff speed.
Fig. S8. Comparison of flapping kinematics before and after impulsive takeoff.
Fig. S9. Robot liftoff demonstration before and after impulsive takeoff.
Fig. S10. Experimental setup.
Fig. S11. Dynamical model and motion-tracking method.
Fig. S12. Robot stability during freefall and swimming.
Table S1. Properties of robot components.
Table S2. Model parameter values.
Movie S1. Demonstration of robot aerial hover.
Movie S2. Demonstration of robot air-water transition.
Movie S3. Demonstration of robot swimming and emergence of robot wing from the water surface.
Movie S4. Demonstration of robot impulsive takeoff and landing.
Movie S5. Comparison of robot underwater stability with different flapping frequencies.
Movie S6. Comparison between robot swimming experiment and simulation.
Movie S7. Measurement of surface tension force on a robot during water-to-air transition.
Movie S8. Comparison of robot takeoff with or without micro-openings on gas collection chamber.
Movie S9. Detonation pressure measurement and robot takeoff.
References (*32*–*35*)

REFERENCES AND NOTES

1. S. Sudo, T. Yano, Y. Kan, Y. Yamada, K. Tsuyuki, Swimming behavior of small diving beetles. *J. Adv. Sci.* **18**, 46–49 (2006).
2. R. J. Lock, R. Vaidyanathan, S. C. Burgess, J. Loveless, Development of a biologically inspired multi-modal wing model for aerial-aquatic robotic vehicles through empirical and numerical modelling of the common guillemot, *Uria aalge*. *Bioinspir. Biomim.* **5**, 046001 (2010).
3. J. Davenport, How and why do flying fish fly? *Rev. Fish Biol. Fish.* **4**, 184–214 (1994).
4. H. Park, H. Choi, Aerodynamic characteristics of flying fish in gliding flight. *J. Exp. Biol.* **213**, 3269–3279 (2010).
5. J. M. V. Rayner, Pleuston: Animals which move in water and air. *Endeavour* **10**, 58–64 (1986).
6. R. R. Murphy, E. Steimle, C. Griffin, C. Cullins, M. Hall, K. Pratt, Cooperative use of unmanned sea surface and micro aerial vehicles at Hurricane Wilma. *J. Field Robot.* **25**, 164–180 (2008).
7. K. Jayaram, J.-M. Mongeau, B. McRae, R. J. Full, High-speed horizontal to vertical transitions in running cockroaches reveals a principle of robustness. *Integr. Comp. Biol.* **50**, E83 (2010).
8. P. Chirarattananon, K. Y. Ma, R. J. Wood, Perching with a robotic insect using adaptive tracking control and iterative learning control. *Int. J. Robot. Res.* **35**, 1185–1206 (2016).
9. M. A. Graule, P. Chirarattananon, S. B. Fuller, N. T. Jafferis, K. Y. Ma, M. Spenko, R. Kornbluh, R. J. Wood, Perching and takeoff of a robotic insect on overhangs using switchable electrostatic adhesion. *Science* **352**, 978–982 (2016).
10. R. Eubank, E. Atkins, G. Meadows, Unattended operation of an autonomous seaplane for persistent surface and airborne ocean monitoring, *Oceans MTS-IEEE Conference*, Seattle, WA, 20 to 23 September 2010 (IEEE, 2010).
11. R. Siddall, M. Kovač, Launching the AquaMAV: Bioinspired design for aerial–aquatic robotic platforms. *Bioinspir. Biomim.* **9**, 031001 (2014).
12. M. M. Maia, P. Soni, F. J. Diez, Demonstration of an aerial and submersible vehicle capable of flight and underwater navigation with seamless air-water transition. http://arxiv.org/abs/1507.01932 (2015).
13. Z. J. Wang, J. M. Birch, M. H. Dickinson, Unsteady forces and flows in low Reynolds number hovering flight: Two-dimensional computations vs robotic wing experiments. *J. Exp. Biol.* **207**, 449–460 (2004).
14. K. Y. Ma, P. Chirarattananon, S. B. Fuller, R. J. Wood, Controlled flight of a biologically inspired, insect-scale robot. *Science* **340**, 603–607 (2013).
15. M. H. Dickinson, F.-O. Lehmann, S. P. Sane, Wing rotation and the aerodynamic basis of insect flight. *Science* **284**, 1954–1960 (1999).
16. Y. Chen, N. Gravish, A. L. Desbiens, R. Malka, R. J. Wood, Experimental and computational studies of the aerodynamic performance of a flapping and passively rotating insect wing. *J. Fluid Mech.* **791**, 1–33 (2016).
17. D. W. Murphy, D. Adhikari, D. R. Webster, J. Yen, Underwater flight by the planktonic sea butterfly. *J. Exp. Biol.* **219**, 535–543 (2016).
18. Y. Chen, E. F. Helbling, N. Gravish, K. Y. Ma, R. J. Wood, Hybrid aerial and aquatic locomotion in an at-scale robotic insect, *IEEE/RSJ International Conference on Intelligent Robots and Systems*, Hamburg, Germany, 28 September to 2 October 2015 (IEEE, 2015), pp. 331–338.
19. J.-S. Koh, E. Yang, G.-P. Jung, S.-P. Jung, J. H. Son, S.-I. Lee, P. G. Jablonski, R. J. Wood, H.-Y. Kim, K.-J. Cho, Jumping on water: Surface tension–dominated jumping of water striders and robotic insects. *Science* **349**, 517–521 (2015).

20. R. J. Wood, S. Avadhanula, R. Sahai, E. Steltz, R. S. Fearing, Microrobot design using fiber reinforced composites. *J. Mech. Des.* **130**, 052304 (2008).
21. Y. Chen, K. Ma, R. J. Wood, Influence of wing morphological and inertial parameters on flapping flight performance, *IEEE/RSJ International Conference on Intelligent Robots and Systems*, Daejeon, South Korea, 9 to 14 October 2016 (IEEE, 2016), pp. 2329–2336.
22. M.-S. Park, Y.-R. Jung, W.-G. Park, Numerical study of impact force and ricochet behavior of high speed water-entry bodies. *Comput. Fluids* **32**, 939–951 (2003).
23. T. M. Wang, X. B. Yang, J. H. Liang, G. C. Yao, W. D. Zhao, CFD based investigation on the impact acceleration when a gannet impacts with water during plunge diving. *Bioinspir. Biomim.* **8**, 036006 (2013).
24. S. Garthe, S. Benvenuti, W. A. Montevecchi, Pursuit plunging by northern gannets (*Sula bassana*) "feeding on capelin (*Mallotus villosus*)." *Proc. Biol. Sci.* **267**, 1717–1722 (2000).
25. D. Vella, J. Li, The impulsive motion of a small cylinder at an interface. *Phys. Fluids* **22**, 052104 (2010).
26. N. T. Jafferis, M. A. Graule, R. J. Wood, Non-linear resonance modeling and system design improvements for underactuated flapping-wing vehicles, *IEEE International Conference on Robotics and Automation*, Stockholm, Sweden, 16 to 21 May 2016 (IEEE, 2016), pp 3234–3241.
27. M. Burrows, Jumping from the surface of water by the long-legged fly *Hydrophorus* (Diptera, Dolichopodidae). *J. Exp. Biol.* **216**, 1973–1981 (2013).
28. D. H. Edwards, G. T. Williams, J. C. Breeze, Pressure and velocity measurements on detonation waves in hydrogen-oxygen mixtures. *J. Fluid Mech.* **6**, 497–517 (1959).
29. D. L. Hu, B. Chan, J. W. M. Bush, The hydrodynamics of water strider locomotion. *Nature* **424**, 663–666 (2003).
30. E. Diller, J. Giltinan, M. Sitti, Independent control of multiple magnetic microrobots in three dimensions. *Int. J. Robot. Res.* **32**, 614–631 (2013).
31. J. P. Whitney, P. S. Sreetharan, K. Y. Ma, R. J. Wood, Pop-up book MEMS. *J. Micromech. Microeng.* **21**, 115021 (2011).
32. N. Nagai, M. Takeuchi, T. Kimura, T. Oka, Existence of optimum space between electrodes on hydrogen production by water electrolysis. *Int. J. Hydrogen Energy* **28**, 35–41 (2003).
33. T. L. Geers, K. S. Hunter, An integrated wave-effects model for an underwater explosion bubble. *J. Acoust. Soc. Am.* **111**, 1584–1601 (2002).
34. M. W. Spong, S. Hutchinson, M. Vidyasagar, Dynamics, in *Robot Modeling and Control* (Wiley, 2006), vol. 3, pp. 239–285.
35. J. P. Whitney, R. J. Wood, Aeromechanics of passive rotation in flapping flight. *J. Fluid Mech.* **660**, 197–220 (2010).

Acknowledgments: We thank J. Koh for comments and discussions. **Funding:** This material is based upon work supported by the NSF (award no. 1537715), an NSF Graduate Research Fellowship under grant no. DGE1144152, and the Wyss Institute for Biologically Inspired Engineering. In addition, the prototypes were enabled by equipment supported by the Army Research Office DURIP program (award no. W911NF-13-1-0311). Any opinions, findings, and conclusions or recommendations expressed in this material are those of the authors and do not necessarily reflect the views of the NSF. **Author contributions:** Y.C. designed the robot. Y.C., H.W., E.F.H., N.T.J., and A.O. conceived the experimental work. Y.C., H.W., E.F.H., R.Z., P.C., and R.J.W. contributed to modeling and data analysis. Y.C. wrote the paper. All authors provided feedback. **Competing interests:** The authors declare that they have no competing interests. **Data and materials availability:** Please contact Y.C. for data and other materials.

Submitted 2 August 2017
Accepted 3 October 2017
Published 25 October 2017
10.1126/scirobotics.aao5619

Citation: Y. Chen, H. Wang, E. F. Helbling, N. T. Jafferis, R. Zufferey, A. Ong, K. Ma, N. Gravish, P. Chirarattananon, M. Kovac, R. J. Wood, A biologically inspired, flapping-wing, hybrid aerial-aquatic microrobot. *Sci. Robot.* **2**, eaao5619 (2017).

Science Robotics

A biologically inspired, flapping-wing, hybrid aerial-aquatic microrobot

Yufeng ChenHongqiang WangE. Farrell HelblingNoah T. JafferisRaphael ZuffereyAaron OngKevin MaNicholas GravishPakpong ChirarattananonMirko KovacRobert J. Wood

Sci. Robot., 2 (11), eaao5619. • DOI: 10.1126/scirobotics.aao5619

Science Robotics (ISSN 2470-9476) is published by the American Association for the Advancement of Science. 1200 New York Avenue NW, Washington, DC 20005. The title *Science Robotics* is a registered trademark of AAAS.